AIAA SciTech Forum
6-10 January 2025, Orlando, FL
AIAA SCITECH 2025 Forum

10.2514/6.2025-1855

Development and Integration of Active Load Control Functions for a High Aspect Ratio Transport Aircraft Simulation

Stefan Langen *, Christina Schreppel †, Felix Stalla ‡, Thiemo Kier §, Özge Süelözgen ¶, and Gertjan Looye ‖
Institute of System Dynamics and Control, German Aerospace Center (DLR), 82234 Weßling, Germany

Hannes Wilke **
Technical University of Berlin (TUB), 10623 Berlin, Germany

The recent efforts to design more environmentally friendly and thus fuel-efficient aircraft have led to wing designs with very high aspect ratios. These designs feature more flexible wings with impacts on safety critical aspects such as reduced flutter speed and higher sensitivity to gusts. To tackle these challenges passive and active functions need to be developed to reduce gust sensitivity and increase flutter speed. This in turn poses new performance requirements on control surface actuators. In the frame of the project wing integrated systems demonstration on mechatronic rig (WISDOM) a hardware in the loop demonstrator is constructed on which newly developed electro mechanical actuator (EMA) will be tested in combination with a simulated aircraft. This aircraft model includes flight dynamics, structural dynamics, and all relevant systems that are not present as hardware. In addition, all relevant control law functions are to be implemented on a separate flight control computer (FCC). This paper describes the development of the integrated real-time capable aircraft model, as well as the flight control function for active alleviation of gust loads. This controller is based on μ-synthesis and is designed to integrate well with primary control functions. To show the successful integration of the primary and secondary control functions nonlinear simulations are presented.

I. Introduction

One of today's main objectives in (civil) transport aircraft design is the reduction of CO_2 emissions. This can be achieved by alternative propulsion, but more likely, by making current designs more fuel efficient. Alternative propulsion methods still need to mature and proof their reliability and safety during operation. But reducing induced drag by increasing the wing aspect ratio is not a novel method and has been done in similar ways even in retrofits for existing designs (e.g. winglet modification). Increasing the aspect ratio is therefore a relatively simple but still effective method to increase efficiency.

Unfortunately, wings with higher aspect ratio are more prone to the effects of gusts and are also less stable with respect to flutter. Therefore, built-in functions for gust load alleviation (GLA) and active load reduction should be included in the controller design for these aircraft.

The topic of active load reduction and flutter suppression has been actively discussed for several decades already. Livne [1] gives a very comprehensive overview of more than 50 years of active flutter suppression (AFS) control. It contains a large bibliography of various different control methods, which have been applied to AFS in the past (e.g. Linear Quadratic Gaussian, pole placement, μ-analysis or fuzzy logic). Flight tests with AFS control of the B-52 control configured vehicle program, the F-4F, F/A-18 and many more are discussed. Also, the outboard aileron modal suppression system (OAMS) for the B747-8, which is a necessary control function for this airplane to damp limit cycle oscillations in some mass configurations, together with the flaps-up vertical modal suppression (F0VMS) in the B787-10, which is responsible for controlling a lowly damped mode, are being looked at.

Regan and Jutte [2] conduct a survey of active control methods for GLA on transport category aircraft. One of the earliest aircraft with active load control was the Lockheed C-5A Galaxy. Due to structural fatigue problems an active lift

*Research Associate, stefan.langen@dlr.de
†Research Associate, christina.schreppel@dlr.de
‡Research Associate, felix.stalla@dlr.de
§Research Associate, thiemo.kier@dlr.de
¶Research Associate, oezge.sueeloezgen@dlr.de
‖Department Head, gertjan.looye@dlr.de
**Research Associate, h.wilke@tu-berlin.de

distribution control system (ALDCS) was implemented. The system reduced the wing root bending moment (WRBM) by more than 30% while remaining below 5% torsional increase [3]. The impact on handling qualities and stability was not significant. In [2] also the load alleviation and ride smoothing (LARS) system, which was tested on the German Aerospace Center (DLR) advanced technologies testing aircraft (ATTAS), is discussed.

Johnston [4] presents a thorough study on the L-1011 TriStar and its maneuver load control (MLC). Maneuver and gust loads and flutter are investigated in laboratory and flight tests and their successful reduction and damping is shown.

In more recent years Bernhammer et al. [5] at the TU Delft show GLA for an unmanned aircraft using variable camber. They achieve up to 50% load reduction. In [6] a feed-forward controller for GLA is developed. They use H_∞ for the control synthesis. A Doppler light detection and ranging (LiDAR) sensor is used to anticipate gusts and successfully reduce structural loads.

Previous work at the institute of System Dynamics and Control (SR) [7] shows a successful implementation of a GLA controller based on μ-synthesis for wind tunnel tests. In [8] and [9] a controller for AFS was demonstrated with promising results during flight tests of a remotely piloted sub-scale demonstrator. Now, those functionalities are tested on full scale hardware of a transport aircraft.

The next step on the way to full-scale flight testing is thus implementing the GLA and load control functions on an actuator test rig in a hardware in the loop (HIL) simulation coupled with the flight control computer (FCC). The actuators are full scale industrial electro mechanical actuator (EMA), specifically designed to feature a high enough bandwidth to support controller functions like GLA and AFS. This task is the goal of the wing integrated systems demonstration on mechatronic rig (WISDOM) project where a hardware rig consisting of three aileron actuators and the respective ailerons is combined with a simulation model of a reference aircraft and the FCC. The overall objective is to run the full setup including the hardware rig with the actuators, the simulation model and the flight controller with primary and secondary functions in real time. This paper is presenting the current status of the WISDOM project with respect to the simulation model and flight controller implementation. The HIL tests are scheduled for 2026. For a more detailed overview of the project see [10].

First, the reference aircraft model, which is used in the simulation, is introduced and described. Then, the controller design for the secondary function (GLA) using μ-synthesis is discussed followed by an overview of the flight controller, which combines both primary and secondary functions. In the end simulation results from preliminary tests on the virtual setup in preparation for the HIL tests are presented.

II. Simulation Model

A. Aircraft Model

The aircraft model used in this paper is a reference model named *D2AE* and was developed by the Institute of Aeroelasticity in the DLR [10, 11]. It is similar to the Airbus A321 short- to mid-haul civil passenger jet. The two main differences are the increased wing span of 42.5 m compared to the one of the A321 (35.8 m) [12]. Additionally, there are three ailerons per wing instead of just one. An overview of the used aircraft model can be seen in Fig. 1 where the separation of the ailerons is shown in more detail. Note, that the spoiler and slats are greyed out in the list because they are not modelled in the reference aircraft. In total there are 15 control surfaces:

- 2 inner flaps
- 2 outer flaps
- 6 ailerons
- 2 elevators
- 1 rudder
- 2 trimmable horizontal stabilizer
- and 2 engines.

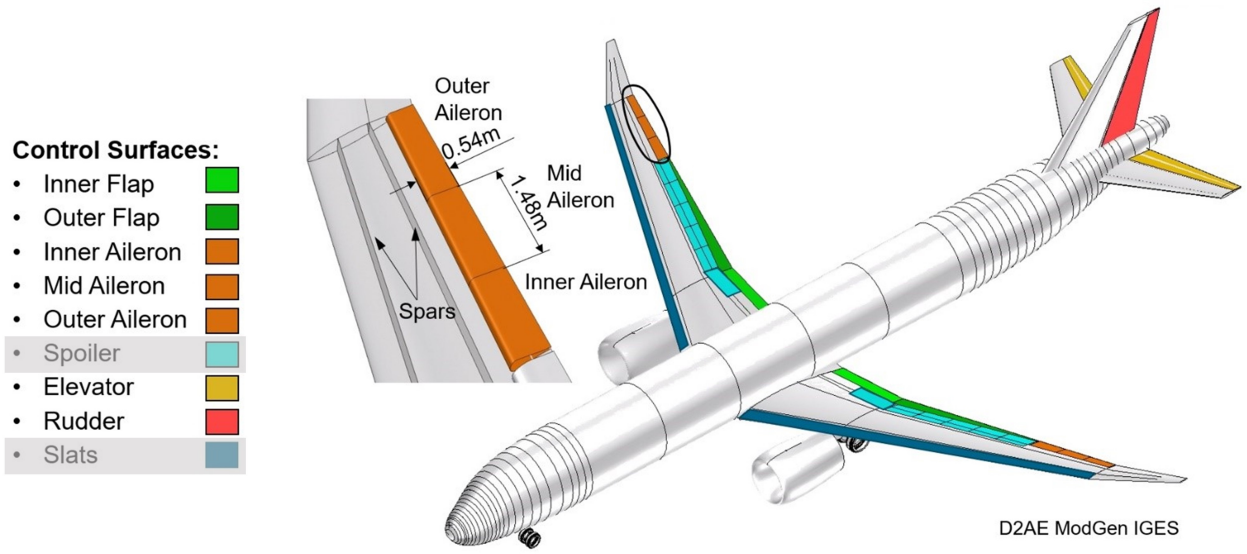

Fig. 1 Aircraft model control surfaces [11]

B. Simulation Model

The mathematical model is generated using the *VarLoads* framework which calculates structural loads with the doublet lattice method [13–15]. Additionally, the Loewner framework [16–18] is used for gust modelling. This leads to a very accurate gust induced loads simulation and is found to be superior to Roger's rational function approximation (RFA) [19]. Further information on the implementation of the gust modelling can be found in [19].

The equations of motion that describe the dynamics of the aircraft flight mechanics and the flexible motion are as follows [15]:

$$\begin{bmatrix} m_\mathrm{b}(\dot{\mathbf{V}}_\mathrm{b} + \boldsymbol{\Omega}_\mathrm{b} \times \mathbf{V}_\mathrm{b} - \mathbf{T}_\mathrm{bE}\,\mathbf{g}_\mathrm{E}) \\ \mathbf{J}_\mathrm{b}\dot{\boldsymbol{\Omega}}_\mathrm{b} + \boldsymbol{\Omega}_\mathrm{b} \times (\mathbf{J}_\mathrm{b}\boldsymbol{\Omega}_\mathrm{b}) \end{bmatrix} = \boldsymbol{\Phi}_\mathrm{bg}\mathbf{P}_\mathrm{g}^\mathrm{ext}(\mathrm{t}), \tag{1}$$

$$\mathbf{M}_\mathrm{ff}\ddot{\mathbf{u}}_\mathrm{f} + \mathbf{D}_\mathrm{ff}\dot{\mathbf{u}}_\mathrm{f} + \mathbf{K}_\mathrm{ff}\mathbf{u}_\mathrm{f} = \boldsymbol{\Phi}_\mathrm{fg}\mathbf{P}_\mathrm{g}^\mathrm{ext}(\mathrm{t}), \tag{2}$$

The first equations describe the flight mechanic motion in rigid body coordinates (*b-set*). The mass (m_b), translational and rotational velocities ($\mathbf{V_b}$, $\mathbf{\Omega_b}$), inertia tensor ($\mathbf{J_b}$) and the gravitational acceleration (g_E) influence the flight mechanic motion. The flexible motion is modelled with the second order matrix differential equation in equation 2 involving the modal matrices for mass ($\mathbf{M_{ff}}$), damping ($\mathbf{D_{ff}}$) and stiffness ($\mathbf{K_{ff}}$). The right hand side of the equations describe the external forces from aerodynamic and atmospheric influences. They are in the time domain and need to be transformed to the modal domain. This is accomplished by the $\mathbf{\Phi_{bg}}$ and $\mathbf{\Phi_{fg}}$ modal matrices.

In the simulation model the number of flexible modes is set to 50 to get a highly detailed model. Additionally, to the monitoring of flexible deformations there are also outputs for the cut loads, which are needed to measure the wing root bending and torsion moments. Also, the hinge moments at all control surfaces and the pressure coefficients (Δc_p) over the control surfaces are calculated.

Since the GLA controller needs vertical acceleration measurements at the wings to determine optimal control deflections a sensor model for the acceleration sensors is developed. In total there are 20 acceleration sensors - 10 at each wing. They are located at the leading and trailing edge and are evenly distributed along the wing span. The acceleration measurement does not only consist of the translational motion but has contributions from:

- translational (center of gravity motion)
- Coriolis (moving of sensor into areas of different rotational speeds)

- tangential (caused by rotation of lever arm)
- centripetal (caused by rotation perpendicular to direction of travel)
- flexible (caused by flexibility of structure)

Actuator models are added to the reference aircraft. In total there are 15 actuators altering the control surface positions. The elevators, flaps and rudder actuators are modeled with 2nd order transfer functions with limits for position (25°) and rate ($60\,^\circ/s$):

$$G_{\text{act}}(s) = \frac{\omega_0^2}{s^2 + 2\zeta\omega_0 s + \omega_0^2} \tag{3}$$

with $\omega_0 = 40$ rad/s and $\zeta = \frac{\sqrt{2}}{2}$. Additionally, there are options to simulate failure cases like position run away.

The other 6 actuator models for the ailerons are modelled in more detail. This model will be provided by the industry partner who is also developing and building the hardware actuator.

In addition to the aircraft model the simulation model also consists of the environment simulation. Here, an atmospheric model passes values for variables like dynamic pressure, temperature or density to the aircraft simulation. Also, gusts and turbulence inputs can be injected as desired.

C. Setup

The final setup for the HIL tests consists of three main parts:

- simulation model on *dSPACE* system
- hardware FCC
- hardware rig

An overview of the setup can be found in Fig. 2. The simulation model is as described in section II.B. Inputs to initialization parameters or gusts can be entered.

The primary and secondary controller functions are part of the FCC. For the HIL tests the FCC will be implemented in hardware. More information about the work on the FCC hardware component can be found in [20, 21]. Pilot inputs can be received either in the form of control inceptor inputs or by injection of command variables through a user interface. The FCC receives sensor data from the simulation model and then calculates the desired control surface deflections. These are passed back to the simulation model and also to the electronic control unit (ECU). The ECU are the local controllers that determine the necessary current for the EMA to deflect to the commanded position. Later on in the project they will also be used to achieve GLA functionality using a local controller at each ECU that uses sensor data directly at the ECU location with a similar method like in [22].

The EMA will then drive the three hardware ailerons in the test rig. Only the ailerons and respective EMA of the right hand side are implemented in the hardware rig (as seen in Fig. 2). The other control surfaces and parts of the aircraft are all simulated in the simulation model. The aerodynamic forces on the right hand side ailerons are simulated by the load actuators, which receive aerodynamic load data from the simulation model.

It is important that the data transfer of the sensor signals from the simulation model, the commanded control surface position from the FCC and the aerodynamic loads are running in sync and with minimal delay. Otherwise, the stability of the system might be compromised. Therefore, the controller area network (CAN) and RS-485 standard are used for time critical data. The user datagram protocol (UDP) is used for not time critical data (e.g. visualization of in- and outputs).

Currently, only software in the loop (SIL) tests are being conducted and HIL tests are scheduled for 2026. The setup is the same as described above with the exception that the three ailerons and actuators of the right wing are currently also in the simulation model and not on a hardware rig. The part, that will be added later on in the project for the HIL tests, is indicated as the greyed out area in Fig. 2.

In order to visualize the flying aircraft and the deflection of the wings a visualization module is added. It receives flight mechanic and structural loads data from the simulation model and also status signals from the FCC.

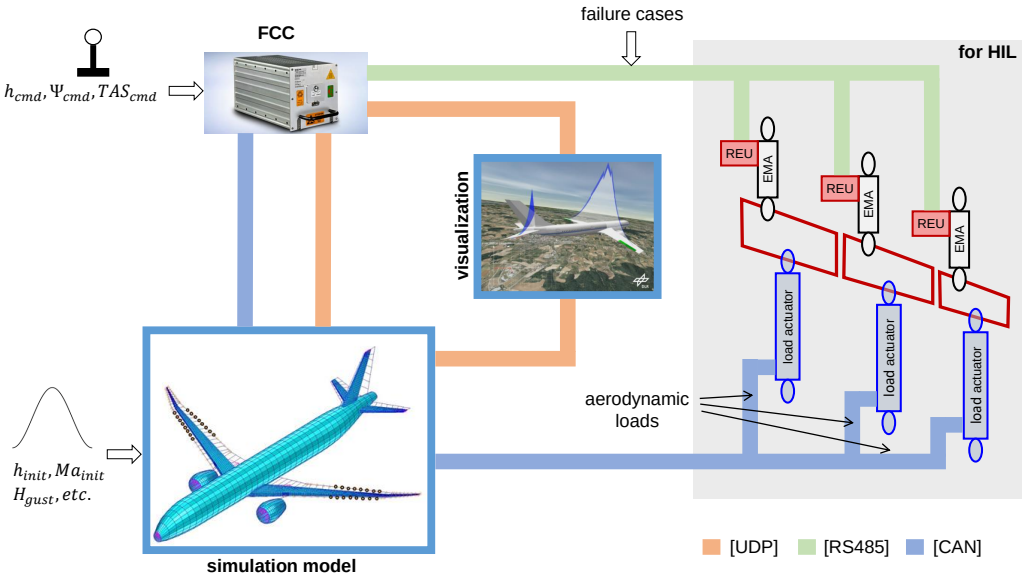

Fig. 2 Overall setup of simulation model, FCC, visualization and hardware rig

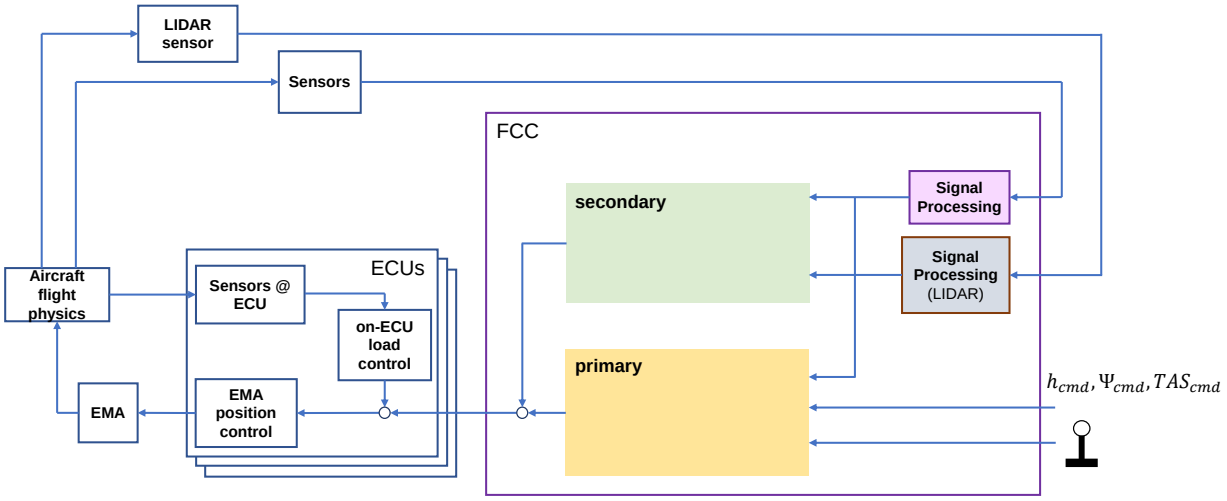

Fig. 3 FCC architecture and closed loop integration

Figure 3 shows the FCC architecture and signals flows. The FCC consists of two main parts - the primary and secondary controller functions. Some of the control functions (e.g. primary flight control, GLA using feed-forward and active flutter suppression) are being developed by other project partners. The primary flight controller was designed in [23] using Eigenstructure assignment. This controller accepts three control variable inputs in automatic flight (altitude, true air-speed and heading commands). Augmented manual flight control is also available but is not used in the application presented here. The primary and secondary control signals are added before being routed to the ECU. No filtering or blending is done. The idea is that by frequency separation of the primary and the GLA controller the interference should be minimal. This is further discussed in section III.B.

The LiDAR sensor is used by the feed-forward GLA controller. The primary flight controller is always active while the secondary functions are switched on and off depending on the test case.

Some of the load alleviation functions, that the FCC is capable of, are also integrated in the ECU [22], as mentioned

earlier in this section. The final architecture will feature a switch to select between local and centralized (i.e. on the FCC) load control to assess the performance of both configurations.

III. Gust Load Alleviation Controller

A. μ-synthesis setup

The GLA controller is designed by using the μ-synthesis approach. With μ-synthesis a robust controller is ensured by design. Because the synthesis algorithms of μ-synthesis work better for smaller sized plants, the simulation model is linearized with only the necessary parts implemented and only the necessary in- and outputs. After the linearization a model order reduction using balanced reduction is applied. Figure 4 shows the μ-synthesis setup. The generalized plant P consists of the aircraft model G including the gust simulation. A gust in vertical direction is chosen for the exogenous input w_G. The real inputs u to the plant consist of the commanded control surface deflections, which are determined by the controller K. The exogenous outputs of the plant consist of the WRBM, wing root torsion moment (WRTM), and also the vertical acceleration measurements at the wings. These outputs, together with the control deflections, are used as the performance outputs e for the synthesis. Weighting functions for the gust W_{gust}, performance outputs W_P, and control deflections W_U allow the designer to shape the H_∞ norm and thus influence the desired closed loop system. In [24] detailed information about μ-Synthesis can be found.

There are 24 performance outputs ($2 \times$ WRBM + $2 \times$ WRTM + $20 \times a_z$). The WRBM and WRTM outputs are needed because they are the key parameters for the load reduction measurement. The a_z values are used to give more information to the optimization. The a_z measurements are indirectly linked to the loads and this way the μ-synthesis can find a solution faster. To normalize the output every channel is divided by its maximum singular value.

The main difference of the generalized plant between H_∞- and μ-synthesis is the addition of uncertainty to the model. This is added by uncertainty Δ_{act} at the control inputs. For the sensor outputs, that are fed to the controller, only selected ones are used. The selection takes place in H_{select} and only the two sensors at the leading edge of the wingtip are used as real outputs of P (y signals). These sensors were picked after tests with only 2 sensors and it was found out that the most load reduction can be achieved with this pair. After the selection in H_{select} the uncertainty Δ_{sens} is added.

Also, only 2 out of 6 ailerons are used in this synthesis. The outer aileron on the left and right wing are chosen because they have the greatest effect on load reduction. The reason for using only a subset of the available acceleration sensors and actuators is the desire to be able to achieve GLA with as few sensors and control surfaces as possible. Also, the computation time for the μ-synthesis is greatly reduced by using only a subset of sensors and actuators because the D scales are of smaller size because of less uncertainty channels. As a next step the performance can be further improved by adding more sensors and control surfaces to the design.

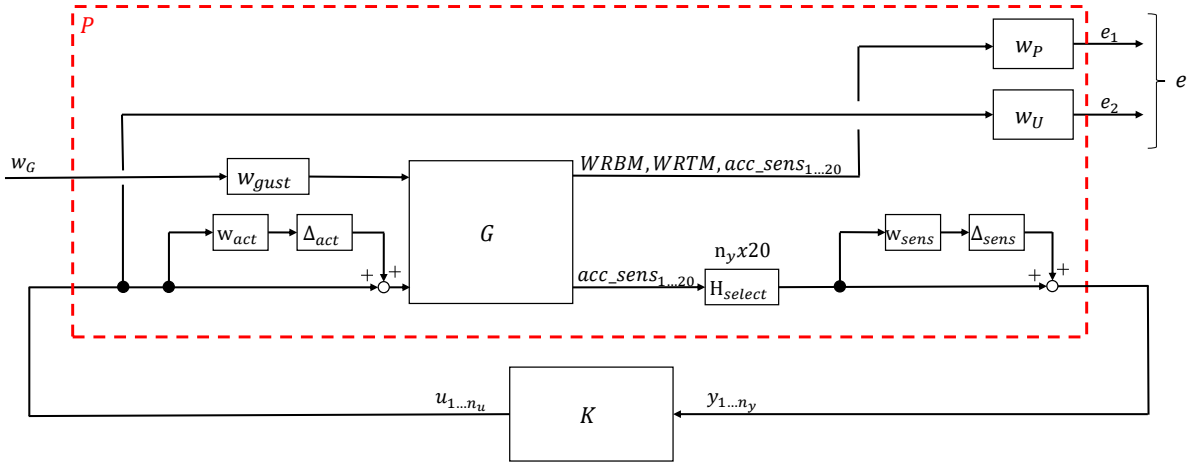

Fig. 4 Overview of μ-synthesis setup. Adapted from [19]

B. Weighting functions

The weighting functions can be found in Fig. 5a. The performance weight W_P has a sharp roll off to lower frequencies, because the GLA controller should not influence the flight mechanic modes which are located around $1 \ldots 2$ rad/s. It also rolls off at higher frequency with the cut-off frequency at the bandwidth of the actuator, because there would be no point in trying to influence a frequency range where the actuator has no effect. All in all the performance weight puts the focus on the area where the flexible modes are located so that the peaks of the H_∞ norm are emphasized in this range. The gust weight W_{gust} is constant. It is the inverse of the peak value of the most critical gust. Like the W_P weight the input weight W_U is focusing on control activity in the range where the flexible modes are. Unlike for the W_P weight there is no roll off to higher and lower frequencies but only a constant gain reduction. The reason is that this would result in infinite gains at low and high frequencies and the optimization would not be able to find a solution. The low frequency gain is higher than the high frequency gain in the W_U weight. This setting was found iteratively to put more weight on restricting the controller to not use the conflicting frequency range of $1 \ldots 2$ rad/s.

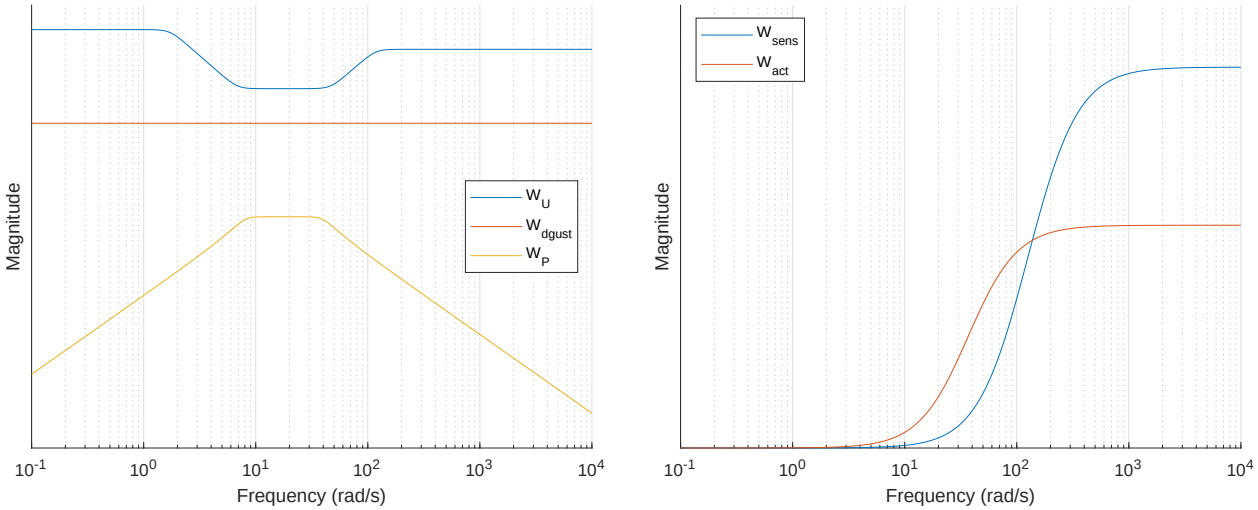

(a) Exogenous in- and outputs weighting functions **(b) Sensitivity weighting functions**

Fig. 5 Weighting functions

Figure 5b shows the weighting functions for the uncertainty in actuators and acceleration sensors. The lower frequency is trusted more than the high frequency range, because this represents real life behavior.

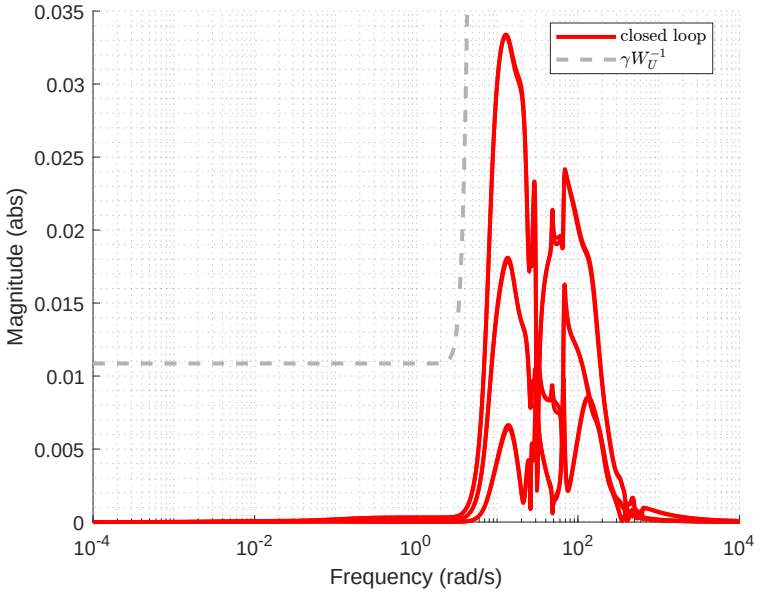

Fig. 6 Closed loop frequency response from gust input to control activity

The resulting closed loop frequency response from a gust input to the control activity can be seen in Fig. 6. The dotted line shows the inverse of the weighting function multiplied with the minimum achievable H_∞-norm (γ).

C. Stability and Robustness

In order to validate the stability of the GLA controller the diskmargins are checked for the input and output margins. Both, multiloop and loop-at-a-time margins are checked. Table 1 shows the margins for input and output cut points. For the multiloop margins the smallest ones are displayed. As expected the multiloop margins are smaller than the loop-at-a-time margins. The worst perturbations of the output cut point is the one of the right wing tip sensor and the worst perturbation of the input cut point is at the left aileron. The diskmargins show that the controller is sufficiently robust.

Table 1 Diskmargins

Type	cut point	gain margin (dB)	phase margin	frequency (rad/s)
multiloop	input	10.4	56.3°	31.5
multiloop	output	10.2	55.6°	31.4
loop-at-a-time	input	13.9	67.1°	31.8
loop-at-a-time	output	13.4	65.7°	32.2

Also, a μ-analysis is conducted. Figure 7 shows the result. The robust stability is well below 1 indicating that the uncertainty in the plant can be increased by the inverse of the peak robust stability value and the closed loop system will still remain stable. On the other hand the nominal and robust performance are also well below 1. This means that there is still room for improvement on the performance side.

The stability of the primary flight controller is shown in [23]. At the time of writing there was no linear model of the primary flight controller available therefore the stability of the coupled controller has been tested by introducing a time delay between the sensor measurements and all sensor inputs to the flight controller. Up to 30 ms time delay have been tested and the closed loop remains stable. It is estimated that the final delay in the hardware FCC and the combined setup together will be $\approx 20\,ms$.

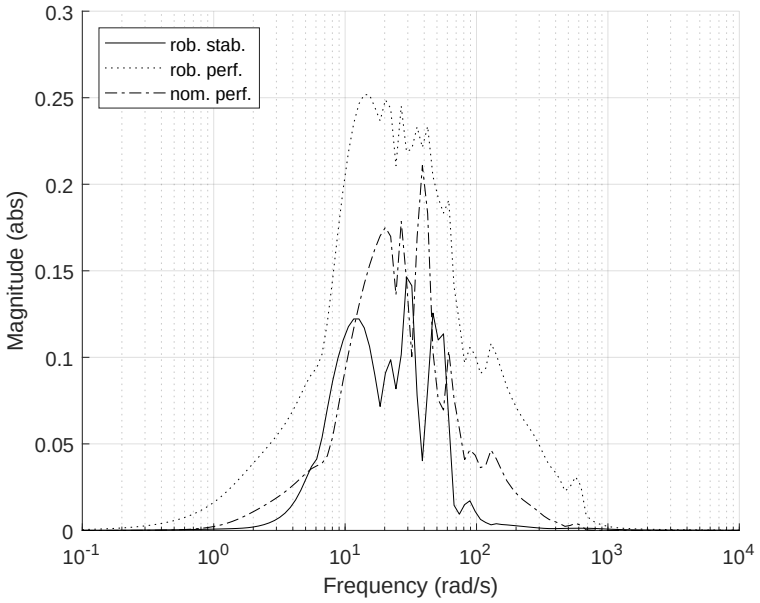

Fig. 7 μ-analysis

IV. Hardware Implementation in Real Time

In preparation for the HIL tests the aircraft model and the controller need to run in real time. The *dSPACE Scalexio* system [25] is used to achieve that. Before the model can be executed on the *dSPACE* system, code needs to be generated from the *Simulink* simulation model. This is done using the provided *dSPACE* software. The $ode5$ Dormand-Prince solver is used with a fixed step size of $0.001s$, which is about $1/10$ of the frequency of the fastest pole in the model. For the simulation the full aircraft model including 50 flexible modes with the flight controllers running is used. In the initial hardware tests the task execution time (TET) ($\approx 0.00065s$) was well below the target step size meaning real time capability is ensured. Figure 8a shows the TET over the simulated time. The changes in TET are most likely due to internal processes in the *dSPACE* hardware.

To ensure that the generated data for the real time simulation on the *dSPACE* system matches the *Simulink* simulation model the differences between various outputs are compared. These include the flexible modes, cut load outputs, control surface deflections and the body rates p, q, r. All variables from the *dSPACE* simulation and the original model match within an error of $\approx 1e-10$. Figure 8b shows the absolute difference of the body rates p, q, r and Fig. 8c the one of the generalized modal coordinates U_f. The increase in difference at the time point of about $1\ s$ is due to the injection of a vertical gust at $t = 1\ s$.

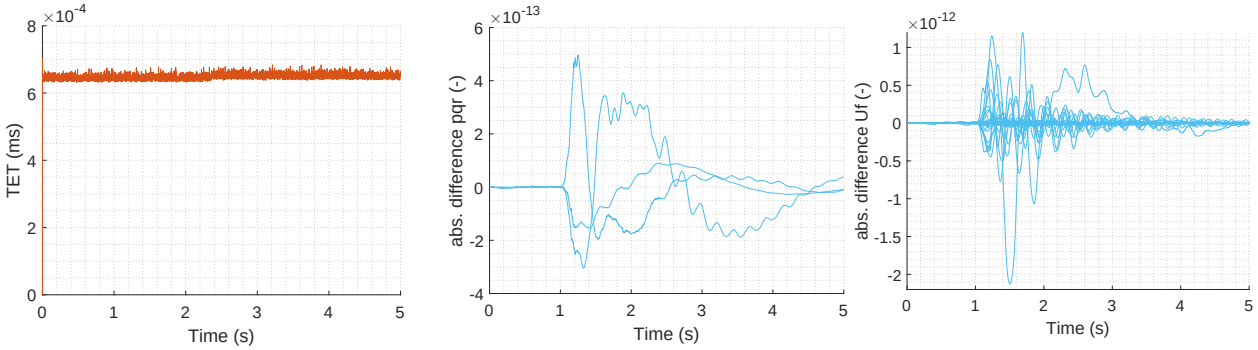

(a) TET **(b) absolute difference p, q, r** **(c) absolute difference U_f**

Fig. 8 *dSPACE* real time simulation

V. Results of Simulation Tests

The goal of the simulation tests is to check the interaction between the trajectory controller and the GLA controller and to assess the interference between them. Overall the expectation is that due to the frequency separation of the GLA controller the interference should be minimal. The GLA controller is designed with a focus on robustness to ensure that the coupling with the primary controller works successfully. After the concept has been proven to be functional further tuning of the controller can be done to achieve a better performance in load reduction. This will also include the addition of more control surfaces.

A. Load Alleviation Performance

For the performance assessment of the GLA controller a 1-cos gust as specified in CS-25.341 [26] is applied. Gust gradients from $H = 10\,m$ to $H = 40\,m$ are used. The controller has not yet been tuned for higher gust gradients and therefore they are not presented in the results.

In Fig. 9 the GLA performance is shown for $H = 10\,m$. The gust is injected at $t = 1\,s$. The closed loop response (green) is plotted on top of the open loop response (red). Both left and right WRBM and WRTM are plotted. The values of WRBM and WRTM are normalized so that the relative reduction of the peak is immediately visible. It can be seen that the peaks of WRBM and WRTM are successfully reduced. The relative reduction of peak WRBM is about 7% and 1% for WRTM. The absolute reduction for WRBM is $25.8 \times 10^3\,Nm$ on the right side and $28.8 \times 10^3\,Nm$ on the left side. The load reduction for WRTM on the right side is $3.2 \times 10^3\,Nm$ and on the left side $0.4 \times 10^3\,Nm$. The asymmetric load reduction is caused by the controller and needs to be further investigated.

Also the control activity is shown for the outer ailerons. The simulation should start in trimmed flight. However, because the actuator model does not yet feature an input for trimmed values a jump can be observed in the initial time steps of the control activity where the actuator is moving to the trimmed value. This also causes the oscillations in WRBM and WRTM as seen in Fig. 9a and 9b. By starting the gust at $t = 1\,s$ and not immediately at $t = 0\,s$ the oscillations have settled down enough.

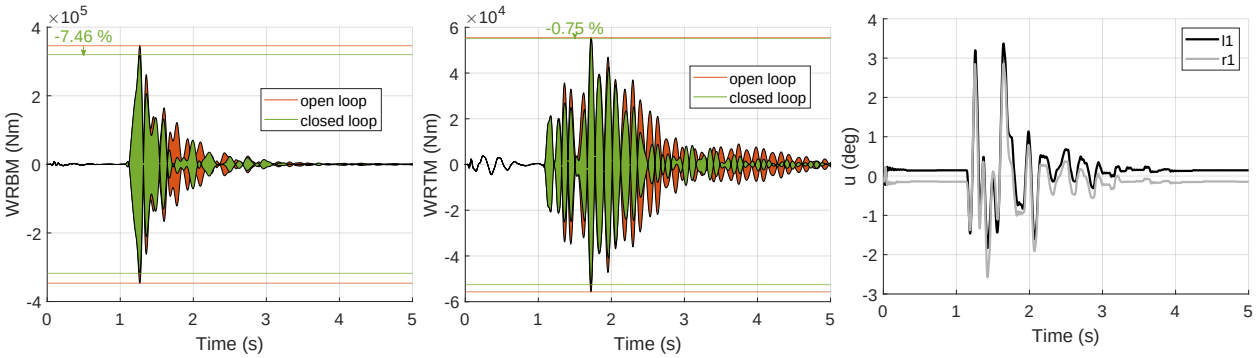

(a) WRBM reduction **(b) WRTM reduction** **(c) control activity**

Fig. 9 Load alleviation performance with 1-cos gust disturbance ($H = 10\,m$)

B. Combined Flight Controller

With the GLA controller being tested successfully the coupled controller, where the primary and secondary control functions are added, can be assessed. Several different maneuvers have been tested to assess the interaction and the performance of each controller in the combined setup (table 2). The maneuvers have been picked to showcase the performance of the trajectory controller and to see the influence of the GLA controller on the execution of these maneuvers. The maneuver ID, commanded altitude change Δh_{cmd}, commanded heading change $\Delta\Psi_{cmd}$ and commanded true air-speed change $\Delta V_{TAS\,cmd}$ are shown. The commanded altitude and heading vary depending on the maneuver but the command value for the true air-speed remains 0 for all maneuvers. A vertical gust with gradients of $H = [10\,m, 40\,m]$ is injected at $t = 1\,s$. Because the standalone GLA performance for $H = 106\,m$ is not yet satisfactory, this gust gradient is not used in the initial testing of the coupled controller.

For every maneuver and gust gradient two simulations are conducted. One with only the primary flight controller active and one where both controllers are turned on. This way the influence of the GLA controller on the performance of

Table 2 Maneuvers commanded values

Name	ID	$\Delta h_{cmd}(m)$	$\Delta\Psi_{cmd}(deg)$	$\Delta V_{TAS\,cmd}(m/s)$
straight and level	1	0	0	0
turn	2	0	10	0
climb	3	200	0	0
climb and turn	4	200	10	0
descent and turn	5	−200	10	0

the primary flight controller can be seen. Figure 10 shows flight mechanic parameters for the climb and turn maneuver ($ID = 4$) with a gust gradient of $H = 40\,m$.

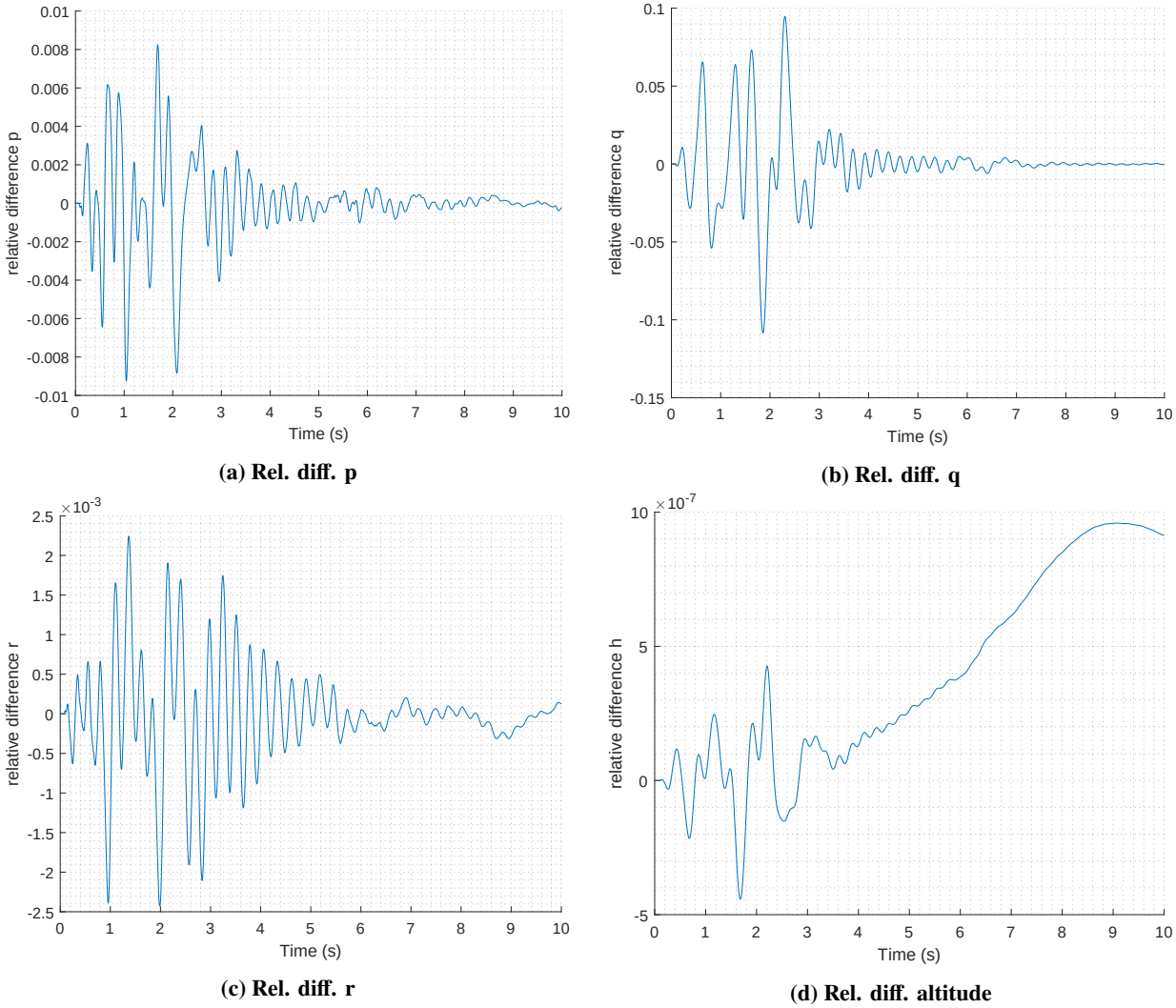

(a) Rel. diff. p

(b) Rel. diff. q

(c) Rel. diff. r

(d) Rel. diff. altitude

Fig. 10 Coupled controller performance in climb and turn maneuver with 1-cos gust disturbance ($H = 40\,m$)

The relative difference of the rigid body rotation rates p, q, r and the altitude h between tests with only the primary controller active and tests with primary and secondary controller active are shown. The relative difference is small and remains < 0.1. Overall it can be seen that the trajectory objectives are mostly uninfluenced by the GLA controller.

The maximum relative difference is present in the rigid body pitch rate q. In Fig. 11 the rigid body rates p, q, r are plotted with only the primary flight controller active (red) and with primary and secondary controller active (green). The green line (coupled controller) of the pitch rate q is more damped than the red line (only primary controller) and this is where the increase in difference for q comes from. The effect is not deemed to be negative but would even improve ride comfort because of less oscillations in the pitch rate.

Figure 12 shows the GLA performance for the coupled controller in the same maneuver as Fig. 10. The vertical accelerations over the wing are damped successfully (see Fig. 12b). The peak WRBM loads seem to be reduced after the gust is injected at $t = 1\,s$ (Fig. 12a).

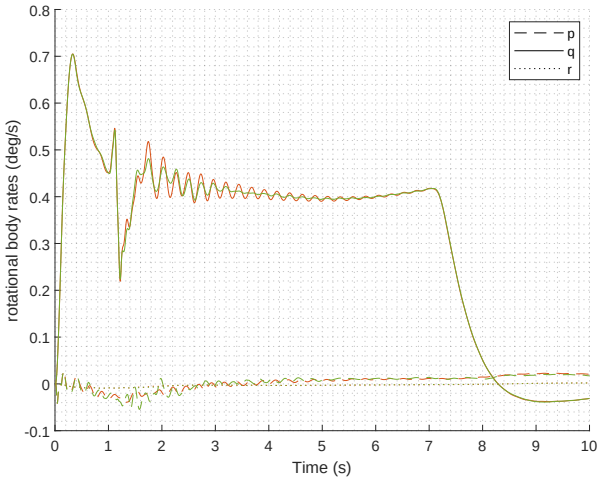

Fig. 11 Rotational rates in climb and turn maneuver with 1-cos gust disturbance ($H = 40\,m$)

To check the actual GLA performance the load reduction is analyzed and the results are shown in table 3. The relative reduction in the peak WRBM resulting from the gust disturbance is hard to measure since the WRBM for the case with GLA turned on is already at a lower level at the time the gust is injected. This is because the GLA controller is already reducing loads in maneuvering flight (but without interference of the trajectory performance as shown in Fig. 10). Therefore, only the absolute load reduction in kNm is given in table 3. Load reduction for both sides (left and right) are shown. A negative value means load reduction and positive means the load is higher with GLA on compared to GLA off. Table 3 only compares the loads during the time when the gust is present ($t = [1, 2]$).

The WRBM loads are successfully reduced for gust gradients $H = [10\,m, 40\,m]$.

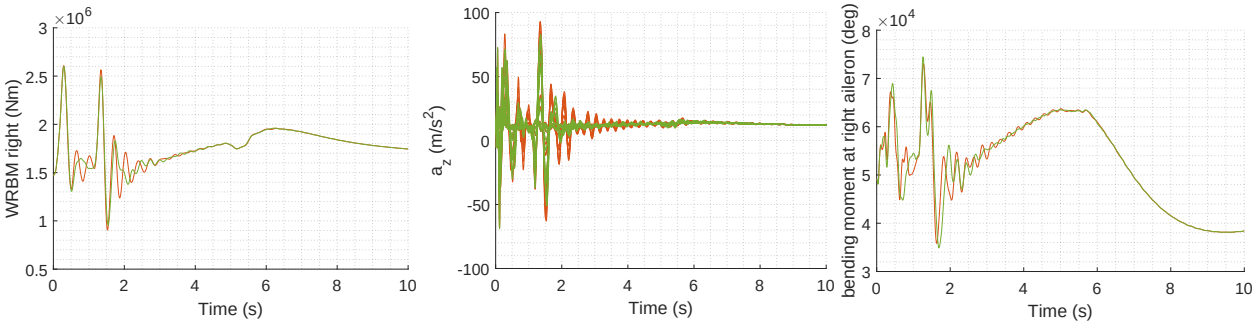

(a) right WRBM **(b) vertical accelerations at wing** **(c) wing bending moment at right aileron**

Fig. 12 Coupled controller load reduction performance in climb and turn maneuver with 1-cos gust disturbance ($H = 40\,m$)

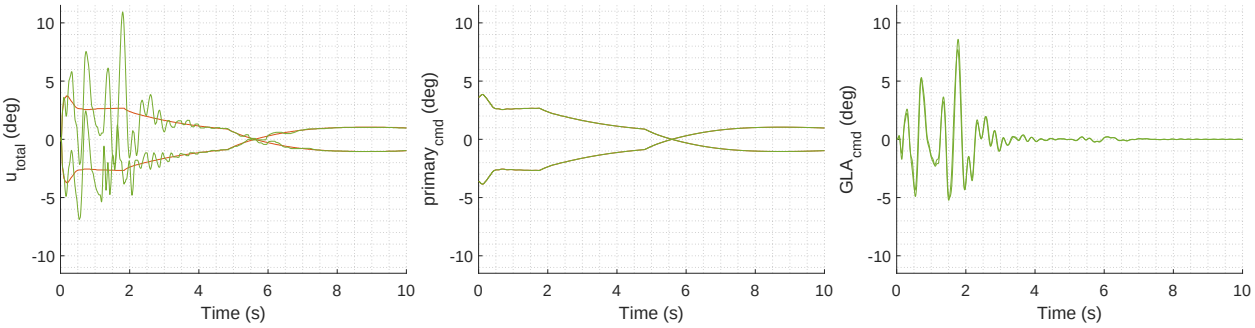

(a) measured outer aileron deflections **(b) primary outer aileron commands** **(c) GLA outer aileron commands**

Fig. 13 Actuator activity for climb and turn maneuver with 1-cos gust disturbance ($H = 40\,m$)

Also the cut loads on the wing close to the ailerons are investigated in Fig. 12c. As expected the cut loads at this position increase when the GLA controller is active. The reason is the introduced bending moment from the aileron deflection that is needed to counteract the gust dynamics. The absolute value change varies between $-0.150\,kNm$ and $1.826\,kNm$ with a mean of $0.906\,kNm$ (see table 3). The increase in loads is still relatively small and therefore not problematic.

The control activity is visualized in Fig. 13. Here the total deflections (Fig. 13a), commanded deflections from the primary flight controller (Fig. 13b) and the commanded deflections from the GLA controller (Fig. 13c) for the outer ailerons are shown. It can be seen in Fig. 13b that primary commands remain mostly the same (green line overlaps red) for the case with GLA turned off (red) and on (green). This also confirms that the interference between primary and secondary flight control is minimal.

Table 3 Coupled GLA performance absolute reduction

gust $H(m)$	maneuver ID	$WRBM$ (left | right) (kNm)	$Pc1_{ail}$ (left | right) (kNm)
10	1	−27.137 | −24.304	0.969 | 0.754
10	2	−54.909 | −48.763	1.542 | 0.130
10	3	−29.906 | −26.924	0.850 | 0.835
10	4	−55.284 | −49.895	1.615 | 0.106
10	5	−47.273 | −40.402	1.308 | −0.150
40	1	−14.374 | −12.461	0.749 | 0.308
40	2	−72.381 | −73.928	1.826 | 1.737
40	3	−13.927 | −12.913	0.557 | 0.081
40	4	−69.628 | −72.225	1.649 | 1.474
40	5	−70.162 | −70.756	1.821 | 1.764

VI. Conclusion

The design of the simulation model and overall setup has been completed. Within this setup, the framework for a GLA controller has been established, with μ-synthesis employed to develop the controller. The primary objective is to test its interaction with the primary flight controller. For the initial configuration, only a limited number of sensors and actuators are utilized. The load reduction performance is satisfactory for shorter gusts, up to $H = 40\,m$. However, for longer gusts, further improvements of the GLA controller tuning are necessary. These enhancements may be achieved through multi-objective optimization, where the weighting functions of the generalized plant are tuned using a high-level optimization routine powered by the multi objective parameter synthesis (MOPS) toolbox [27, 28].

The interactions between the primary and secondary flight control functions have been evaluated. Overall, the GLA controller has minimal influence on the trajectory performance of the primary flight controller. This is achieved through

frequency separation in the GLA controller design. The control activity weight is shaped to avoid control actions in the range of flight mechanics modes, allowing the GLA controller to perform its tasks with minimal interference with the primary flight controller operations.

Real-time capability has been successfully tested on the *dSPACE Scalexio* system. This industry-grade real-time platform enables the aircraft model and all controllers to operate in real-time with a buffer exceeding 50%.

The overall setup of the coupled controller, integrating both primary and secondary functions, has been validated successfully. The next steps involve tuning the GLA controller gains to improve performance further. Additional control surfaces will be integrated into the process. Additionally, in preparation for HIL tests, more hardware components are being incorporated into the setup to evaluate software-hardware interactions effectively.

Acknowledgments

The underlying work in the joint project WISDOM was carried out within the framework of the aviation research program (LuFo VI-2) and funded under the funding code 20Y2105 by the German Federal Ministry of Economics and Climate Protection (BMWK) on the basis of a resolution of the German Bundestag.

The authors would like to thank the project partners at the Technical University of Berlin for supplying their primary flight controller for this investigation. And the Institute for Flight Systems in DLR (DLR-FT) for their support in the real time implementation.

The reference aircraft model was designed at the Institute of Aeroelastics, department Loads Analysis and Aeroelastic Design in DLR (DLR-AE-LAE) [11].

References

[1] Livne, E., "Aircraft Active Flutter Suppression: State of the Art and Technology Maturation Needs," *Journal of Aircraft*, Vol. 55, No. 1, 2018, pp. 410–452. https://doi.org/10.2514/1.c034442.

[2] Regan, C. D., and Jutte, C. V., "Survey of Applications of Active Control Technology for Gust Alleviation and new Challenges for Lighter-Weight Aircraft," Tech. rep., 2012.

[3] Disney, T. E., "C-5A Active Load Alleviation System," *Journal of Spacecraft and Rockets*, Vol. 14, No. 2, 1977, pp. 81–86. https://doi.org/10.2514/3.57164.

[4] Johnston, J., "Accelerated Development and Flight Evaluation of Active Controls Concepts for Subsonic Transport Aircraft. Volume 1: Load Alleviation/Extended Span Development and Flight Tests," Tech. rep., 1979.

[5] Bernhammer, L. O., Teeuwen, S. P., De Breuker, R., van der Veen, G. J., and van Solingen, E., "Gust Load Alleviation of an Unmanned Aerial Vehicle Wing Using Variable Camber," *Journal of Intelligent Material Systems and Structures*, Vol. 25, No. 7, 2014, pp. 795–805.

[6] Khalil, A., and Fezans, N., "Gust Load Alleviation for Flexible Aircraft Using Discrete-Time Preview Control," *The Aeronautical Journal*, Vol. 125, No. 1284, 2020, pp. 341–364. https://doi.org/10.1017/aer.2020.85.

[7] Stalla, F., Looye, G., Kier, T., Michel, K., Schmidt, T. G., Hanke, C., Kirmse, T., and Pusch, M., "Wind Tunnel Assessment of a Robust Gust Load Alleviation Controller Designed Using μ-Synthesis," *AIAA SCITECH 2025 Forum*, American Institute of Aeronautics and Astronautics, 2025.

[8] Kier, T., Wüstenhagen, M., Süelözgen, O., Konatala, R., Meddaikar, Y., Soal, K., Guerin, N., Bartasevicius, J., Takarics, B., Balogh, D., and Vanek, B., "Aeroservoelastic models for design, testing, flight test clearance and validation of active flutter suppression control laws," , Jun. 2024. URL https://www.ifasd2024.nl/conference-programme/.

[9] Wuestenhagen, M., "Synthesis of a Multiple-Model Adaptive Gust Load Alleviation Controller for a Flexible Flutter Demonstrator," *AIAA SCITECH 2022 Forum*, American Institute of Aeronautics and Astronautics, 2022. https://doi.org/10.2514/6.2022-0440.

[10] Schumann, H., Lübbe, S. M., Klimmek, T., and Quero, D., "Prüfstand für multifunktionale Flugsteuerungssysteme zur Lastminderung und Flatterunterdrückung bei Verkehrsflugzeugen," *Deutscher Luft- und Raumfahrtkongress (DLRK)*, 2023. URL https://elib.dlr.de/198700/.

[11] Klimmek, T., Schulze, M., and Wöhler, S., "Development of a Short Medium Range Aircraft Configuration for Aeroelastic Investigations using cpacs-MONA," *Deutscher Luft- und Raumfahrtkongress (DLRK)*, 2022. URL https://elib.dlr.de/194675/.

[12] "Type-Certificate-Data Sheet," Tech. Rep. No. EASA.A.064 for AIRBUS A318 - A319 - A320 - A321, European Union Aviation Safety Agency (EASA), 2024.

[13] Hofstee, J., Kier, T., Cerulli, C., and Looye, G., "A Variable, Fully Flexible Dynamic Response Tool for Special Investigations (VarLoads)," *International Forum on Aeroelasticity and Structural Dynamics (IFASD)*, 2003.

[14] Kier, T., and J., H., "VarLoads - eine Simulationsumgebung zur Lastenberechnung eines voll flexiblen, freifliegenden Flugzeugs," *Deutscher Luft- und Raumfahrtkongress (DLRK)*, 2004.

[15] Kier, T., and Looye, G., "Unifying manoeuvre and gust loads analysis," *International Forum on Aeroelasticity andStructural Dynamics (IFASD)*, 2009. URL https://elib.dlr.de/97798/1/IFASD-2009-106.pdf.

[16] Mayo, A., and Antoulas, A., "A framework for the solution of the generalized realization problem," Vol. 425, No. 2–3, 2007, pp. 634–662. https://doi.org/10.1016/j.laa.2007.03.008.

[17] Antoulas, A. C., Lefteriu, S., and Ionita, A. C., *Chapter 8: A Tutorial Introduction to the Loewner Framework for Model Reduction*, Society for Industrial and Applied Mathematics, 2017, pp. 335–376. https://doi.org/10.1137/1.9781611974829.ch8.

[18] Karachalios, D. S., Gosea, I. V., and Antoulas, A. C., *6 The Loewner framework for system identification and reduction*, De Gruyter, 2021, pp. 181–228. https://doi.org/10.1515/9783110498967-006.

[19] Stalla, F., Kier, T. M., Looye, G., and Pusch, M., "Aeroservoelastic Modeling and Robust Control for Gust Load Alleviation of an Experimental Wing," *AIAA SCITECH 2024 Forum*, American Institute of Aeronautics and Astronautics, 2024. https://doi.org/10.2514/6.2024-1442.

[20] Nöldeke, P., Lukić, B., and Durak, U., "FPGA-Based Fault Tolerance Framework for Avionics Systems," *2024 AIAA DATC/IEEE 43rd Digital Avionics Systems Conference (DASC)*, IEEE, 2024, pp. 1–7. https://doi.org/10.1109/dasc62030.2024.10749033.

[21] Lukić, B., Nöldeke, P., Durak, U., Klimmek, M., Jakob, S., and Gläser, M., "From Architecture Models to a Target Platform: A Systematic Approach to Model-Driven Development of Dynamically Reconfigurable Avionics Systems," *2024 AIAA DATC/IEEE 43rd Digital Avionics Systems Conference (DASC)*, IEEE, 2024, pp. 1–10. https://doi.org/10.1109/dasc62030.2024.10749454.

[22] Michel, K., Stalla, F., Looye, G., Schmidt, T. G., and Hanke, C., "Experimental Validation of Decentralized Control for Gust Load Alleviation in a Wind Tunnel," *AIAA SCITECH 2025 Forum*, American Institute of Aeronautics and Astronautics, 2025.

[23] Wilke, H., Silva, G. C., and Silvestre, F. J., "Aileron-Flap-Integrated Roll Control Law By Optimized Control Allocation For Flexible Transport Aircraft," *ICAS*, 2024.

[24] Bennani, S., Looye, G., and Mulder, J., "RCAM Design Challenge Presentation Document: the μ-Synthesis Approach," *GARTEUR*, 1997.

[25] "SCALEXIO System," , 2024. URL https://www.dspace.com/en/ltd/home/products/hw/simulator_hardware/scalexio.cfm, last visited on 2024-11-29.

[26] European Union Aviation Safety Agency (EASA), "Certification Specifications and Acceptable Means of Compliance for Large Aeroplanes (CS-25)," 2023. Amendment 28.

[27] Joos, H.-D., "Multi-objective parameter synthesis (MOPS)," *Robust Flight Control*, edited by J.-F. Magni, S. Bennani, and J. Terlouw, Springer Berlin Heidelberg, Berlin, Heidelberg, 1997, pp. 199–217. https://doi.org/10.1007/BFb0113860.

[28] Joos, H.-D., Bals, J., Looye, G., Schnepper, K., and Varga, A., "A multi-objective optimisation-based software environment for control systems design," 2002. URL https://elib.dlr.de/11882/.